Yu *et al. Energy Mater.* **2025**, *5*, 500086
DOI: 10.20517/energymater.2024.268

Energy Materials

Article

Open Access

Check for updates

Three-dimensional MXene coupled CoFe nanoalloys as sulfur host for long-life room-temperature sodium-sulfur batteries

Xiaoming Yu[1,2], Hao Li[1], Kuan Liang[1], Shengdong Liu[3], Liuqing Li[1], Ye Zhu[1], Haitao Huang[1,2,*]

[1]Department of Applied Physics, The Hong Kong Polytechnic University, Hong Kong 999077, China.
[2]The Research Institute for Smart Energy, The Hong Kong Polytechnic University, Hong Kong 999077, China.
[3]School of Materials and Energy, Guangdong University of Technology, Guangzhou 510006, China.

[*]**Correspondence to:** Prof. Haitao Huang, Department of Applied Physics, The Hong Kong Polytechnic University, Hung Hom, Kowloon, Hong Kong 999077, China. E-mail: aphhuang@polyu.edu.hk

How to cite this article: Yu, X.; Li, H.; Liang, K.; Liu, S.; Li, L.; Zhu, Y.; Huang, H. Three-dimensional MXene coupled CoFe nanoalloys as sulfur host for long-life room-temperature sodium-sulfur batteries. *Energy Mater.* **2025**, *5*, 500086. https://dx.doi.org/10.20517/energymater.2024.268

Received: 30 Nov 2024 **First Decision:** 8 Jan 2025 **Revised:** 23 Jan 2025 **Accepted:** 10 Feb 2025 **Published:** 22 Apr 2025

Academic Editor: Ho Seok Park **Copy Editor:** Ping Zhang **Production Editor:** Ping Zhang

Abstract

Room-temperature sodium-sulfur (RT Na-S) batteries are potential candidates for next-generation energy storage systems because of low-cost resources, high theoretical capacity, and high energy density. However, their commercialization is hindered by the inherent shuttle effect, insulation of sulfur, and slow catalytic conversion. This study proposes a novel approach involving the design of a C/CoFe alloy catalyst coupled with $Ti_3C_2T_x$ MXene substrate (C/CoFe-MXene) as a three-dimensional porous conductive sulfur host. Polysulfide adsorption/catalytic experiments and density functional theory calculation confirmed the excellent affinity and strong catalytic conversion ability of the C/CoFe-MXene composite for polysulfides. The heterostructure formed between the CoFe alloy and the MXene substrate promotes Na^+ transport and accelerates reaction kinetics of sulfur species. Consequently, the assembled RT Na-S batteries with a C/CoFe-MXene sulfur host (2.0 mg cm^{-2}) deliver a high initial specific capacity of 572 mAh g^{-1} at 1 C. Even at 5 C, the battery achieves ultralong-term cycling over 5,400 cycles with a capacity retention rate of 61.9%, corresponding to a slow capacity fading rate of 0.0089% per cycle, demonstrating outstanding high-rate tolerance. This work provides new insights into the preparation of three-dimensional porous sulfur cathodes with high specific surface area and excellent catalytic activity using catalysts loaded on MXene substrates in RT Na-S batteries.

Keywords: $Ti_3C_2T_x$ MXene, CoFe alloy, 3D porous structure, heterostructures, RT Na-S batteries

INTRODUCTION

Lithium-ion batteries nowadays have been widely used in various fields due to the merit of high energy densities. However, lithium resources are relatively scarce in the earth's crust, showing ever-increasing cost, making it difficult to meet the long-term market requirements[1,2]. Room-temperature sodium-sulfur (RT Na-S) batteries, as an emerging energy storage technology, are expected to solve the above issues of lithium-ion batteries since the sulfur cathode and sodium anode are earth-abundant materials and the assembled RT Na-S batteries also deliver high energy density (1,274 Wh kg^{-1}) and high specific capacity (1,675 mAh g^{-1})[3,4]. However, the practical application of RT Na-S batteries is hindered by fast capacity decay with cycling, which is caused by insulating nature and slow redox kinetics of sulfur, big volume expansion (170%) upon sodiation at the cathode, and polysulfide dissolution along with shuttling during charge/discharge process[5].

The most popular strategy to address the problems is encapsulating sulfur into host materials, forming a composite cathode. For example, nanostructured carbon materials, including carbon nanotubes, carbon nanofibers, hollow carbon nanospheres, *etc.*, were exploited to serve as sulfur hosts to boost the electrical conductivity of the cathode and provide confinement for intermediate reaction products of polysulfides in RT Na-S batteries[6,7]. However, carbon materials only have weak interactions with polysulfides due to their non-polar nature, which contributes to limited suppression of polysulfide shuttling[8]. Therefore, the sulfiphilic transition metal oxides[9], nitride[10], sulfides[11-13] and alloys[14] nanomaterials were introduced into the nanosized porous carbon to further enhance the electrochemical properties of RT Na-S batteries. This is because the newly incorporated components not only exhibit superior chemical adsorption ability to polysulfides but also catalyze the conversion of polysulfides. Therefore, qualified sulfur host candidates for RT Na-S batteries should be equipped with the features below: (a) high specific surface area for loading a desired sulfur amount and relieving the volume change during the charge/discharge process, (b) strong adsorption ability of reaction intermediates to suppress their shuttling, and (c) high electrical conductivity and good catalytic performance for accelerated conversion kinetics at the cathode.

MXenes are a new kind of two-dimensional transition metal carbides/nitrides with the general composition $M_{n+1}X_nT_x$, where M represents transition metal elements (Ti, V, Mo Cr, V, *etc.*), X is carbon and/or nitrogen, and T refers to surface functional groups (-O, -F and -OH). They are equipped with polar functional groups, metallic conductivity and catalytic properties for polysulfides, which makes them potential sulfur hosts for RT Na-S batteries[15]. Multi/few-layer $Ti_3C_2T_x$ MXene and MXene-based composites with heterostructure have been studied as sulfur hosts in RT Na-S batteries and displayed excellent electrochemical performance[16,17]. Nevertheless, restacking and agglomeration of MXene sheets impede the availability of surface-active sites for anchoring and catalyzing sodium polysulfides (NaPSs)[18-20].

Herein, we prepared three-dimensional porous C/CoFe-MXene composites via a combination of electrostatic self-assembly, co-precipitation and pyrolysis. The introduced CoFe alloy not only inhibits MXene restacking but also serves as new active sites to boost the chemical adsorption and catalytic conversion of polysulfides. By virtue of the synergistic effect of the components, the RT Na-S batteries with the C/CoFe-MXene cathode under 2.0 mg cm^{-2} of sulfur loading display a great specific capacity of 572 mAh g^{-1} and retained a reversible capacity of 302 mAh g^{-1} after 700 cycles at 1.0 C, corresponding to a slow capacity fading rate of 0.0912% per cycle. Notably, at 5 C, the C/CoFe-MXene cathode delivered a capacity of 310 mAh g^{-1} and retained a reversible capacity of 192 mAh g^{-1} over 5,400 cycles. It is unraveled that the heterostructure between the CoFe alloy and $Ti_3C_2T_x$ MXene was formed through a Ti-O-M (M=Co, Fe) bond, which facilitates rapid electron transport and accelerates reaction kinetics of sulfur species.

EXPERIMENTAL

Material synthesis

Synthesis of few-layer MXene dispersions and powder

First, 1.6 g lithium fluoride was added to hydrochloric acid solution (20 mL, 9 M) on a Teflon bottle. After stirring thoroughly, Ti_3AlC_2 powder (1 g) was added to the above mixture solution slowly and further stirred at 40 °C for 32 h. The resultant product was washed repetitively via 3,500 rpm centrifugation procedures until the pH of the supernatant reached 6. We then added an appropriate amount of deionized (DI) water, transferred the obtained clay-like deposits to a gas washing bottle and treated it by low-temperature ultrasonication for 1 h under argon atmosphere to delaminate MXene. Finally, a few-layer MXene dispersion was obtained by centrifugation (3,500 rpm, 30 min). In our experiment, around 16 mg mL^{-1} MXene solution was eventually obtained. A portion of the dispersion was freeze-dried to obtain the few-layer MXene powder.

Synthesis of C/CoFe-MXene and C/CoFe

Typically, 0.3 mmol of $Co(NO_3)_2 \cdot 6H_2O$ and 0.45 mmol of $Na_3C_6H_5O_7 \cdot 2H_2O$ were dissolved into 20 mL of DI water. Subsequently, the few-layer MXene dispersion (80 mg, 20 mL) was added to the above mixture solution and stirred for 10 min to obtain solution A. Additionally, 0.2 mmol of $K_3Fe(CN)_6$ was added into 40 mL DI water as solution B, which was further added slowly into solution A with vigorous stirring. The collected precipitation was aged at room temperature for 24 h after continuously stirring for 10 min. Next, the CoFePBA-MXene precursor was washed by filtration. Then, the following powder was dispersed in DI water and further freeze-dried. Finally, The C/CoFe-MXene composite was prepared by pyrolysis of the precursor at 500 °C for 4 h with a heating rate of 3 °C min^{-1} in flowing argon. The synthesis process of C/CoFe alloy is similar to that of C/CoFe-MXene except for the addition of the few-layer MXene dispersion. The formation of the CoFe-PBA follows the reaction below:

$$3Co(NO_3)_2\ (l) + 2K_3[Fe(CN)_6]\ (l) \rightarrow Co_3[Fe(CN)_6]_2\ (s) + 6KNO_3\ (l) \quad (1)$$

Synthesis of S composites

The sulfur composites were prepared through a typical melt diffusion strategy. The as-prepared samples were first mixed with a mass ratio of 7:3 (S:C/CoFe-MXene) by hand milling. The resultant mixture was heated at 155 °C for 12 h in a tube furnace and further heated to 200 °C for 20 min in argon atmosphere to obtain the C/CoFe-MXene/S composite. The C/CoFe/S and MXene/S were prepared under the same conditions.

Material characterization

Structure investigation

X-ray diffraction (XRD) measurements were performed on a diffractometer (Rigaku SmartLab) with Cu Kα source (λ = 0.15406 nm). X-ray photoelectron spectroscopy (XPS, Thermo Fisher ESCALAB 250Xi) was operated to obtain the chemical state of the samples. Field emission scanning electron microscopy (SEM, JEOL Model JSM-6490) and transmission electron microscopy (TEM, JEOL JEM-2100F) with energy-dispersive X-ray spectroscopy (EDS) analysis were used to study the morphology, structure and element distribution. Raman spectra were collected by a WITEC confocal Raman system (Alpha300 R). A Micromeritics ASAP2020 analyzer was used to investigate the surface area and pore structure. Thermogravimetric analysis (TGA) was carried out using a thermogravimetric analyzer [TGA/differential scanning calorimetry (DSC) 3+/1600HT] with a heating rate of 10 °C min^{-1} in nitrogen atmosphere.

Electrochemical measurements

S composites, super P, and sodium carboxymethylcellulose (mass ratio = 7:2:1 in DI water) were mixed into a uniform slurry and then coated onto an Al foil. The electrodes were cut into disks with a diameter of

12 mm after vacuum drying at 60 °C for 12 h, whose normal area sulfur loading is 1.8-2.0 mg cm^{-2} and high area sulfur loading is about 4.5 mg cm^{-2}. The CR2032 coin cells were assembled in an Ar-filled glove box using sodium foil as the anode and a GF/D glass fiber as the separator. The electrolyte was 1.0 M $NaClO_4$ in ethylene carbonate (EC): propylene carbonate (PC) (volume ratio = 1:1) with 5% fluoroethylene carbonate additives (FEC). The galvanostatic discharge/charge and the galvanostatic intermittent titration technique (GITT) measurements of the assembled RT Na-S batteries were tested between 0.5 V and 2.8 V at 25 °C on a program-controlled test system (Shenzhen Neware Battery Co., China). The SOLARTRON electrochemical workstation was used to characterize the cyclic voltammetry (CV) and electrochemical impedance spectroscopy (EIS) measurements.

Na_2S_6 solution adsorption experiment

The Na_2S_6 solution was prepared by sulfur and anhydrous Na_2S powder with the molar ratio of 5:1 in a mixed solvent of EC: PC (v/v 1:1). Then, the suspension was stirred vigorously for 24 h at 80 °C in the argon-filled glove box. Finally, a 0.2 M brown Na_2S_6 solution was obtained. The different samples with the same mass were added into the as-prepared low concentration Na_2S_6 solution. The colors of the solutions after standing overnight were recorded by a digital camera and were further measured by ultraviolet-visible (UV-Vis) absorption spectra.

Symmetrical cell measurements

The two identical electrodes with the active sample were used as working and counter electrodes to construct a CR2032 coin cell with a GF/D glass fiber as the separator, and as-prepared Na_2S_6 solution as electrolyte. The CV tests of symmetrical cells were performed at the scan rates from1 to 10 mV s^{-1} between -1.0 V and 1.0 V.

Linear sweep voltammetry measurement of Na_2S oxidation

A uniform ink was obtained by ultrasonically mixing 5 mg electrocatalyst, 700 μL anhydrous ethanol, 300 μL DI water and 50 μL Nafion. Then, 10 μL ink was dropped onto the glass carbon with an area of 0.196 cm^{-2} and dried to form a working electrode. A platinum wire and a saturated Ag/AgCl electrode were used as the counter electrode and reference electrode, respectively. The electrolyte was obtained by dissolving 0.1 M Na_2S in methanol solution. The linear sweep voltammetry (LSV) curves were measured at a scan rate of 50 mV s^{-1}.

RESULTS AND DISCUSSION

Figure 1A schematically depicts the fabrication procedure of the C/CoFe-MXene. First, few-layer MXene was obtained by selective etching of layered Ti_3AlC_2 MAX [Supplementary Figure 1A] and a further delamination[21,22]. A drop of $Ti_3C_2T_x$ aqueous solution was coated onto a copper film to observe the morphology of MXene sheets. The diameter of most of the 2D sheets is of a few micrometers [Supplementary Figure 1B] and the restacking between sheets was universally observed [Supplementary Figure 1C], which is attributed to Van der waals interaction. Subsequently, cobalt ions are electrostatically adsorbed on the surface of MXene, while the $[Fe(CN)_6]^{3-}$ is added and co-precipitated with Co^{2+} to form CoFe-Prussian blue analogs (PBA) on the surface of MXene. In Figure 1B and Supplementary Figure 2A, the resultant CoFe-PBA in the shape of nano cubes (~200 nm) is uniformly distributed on MXene surface. The CoFe-PBA was then transformed into C/CoFe alloy nanoparticles via pyrolysis. Supplementary Figure 2B-D demonstrates that the formed C/CoFe alloy is a nanosphere with a core-shell structure and a size of about 60 nm, in which the alloy is the core, and the carbon layer is the shell, and the overall morphology is accompanied by reunion. In contrast, Figure 1C and D shows that C/CoFe alloy is evenly distributed on the MXene substrate, which is effective to prohibit the restacking of MXene. To be more specific, the high-

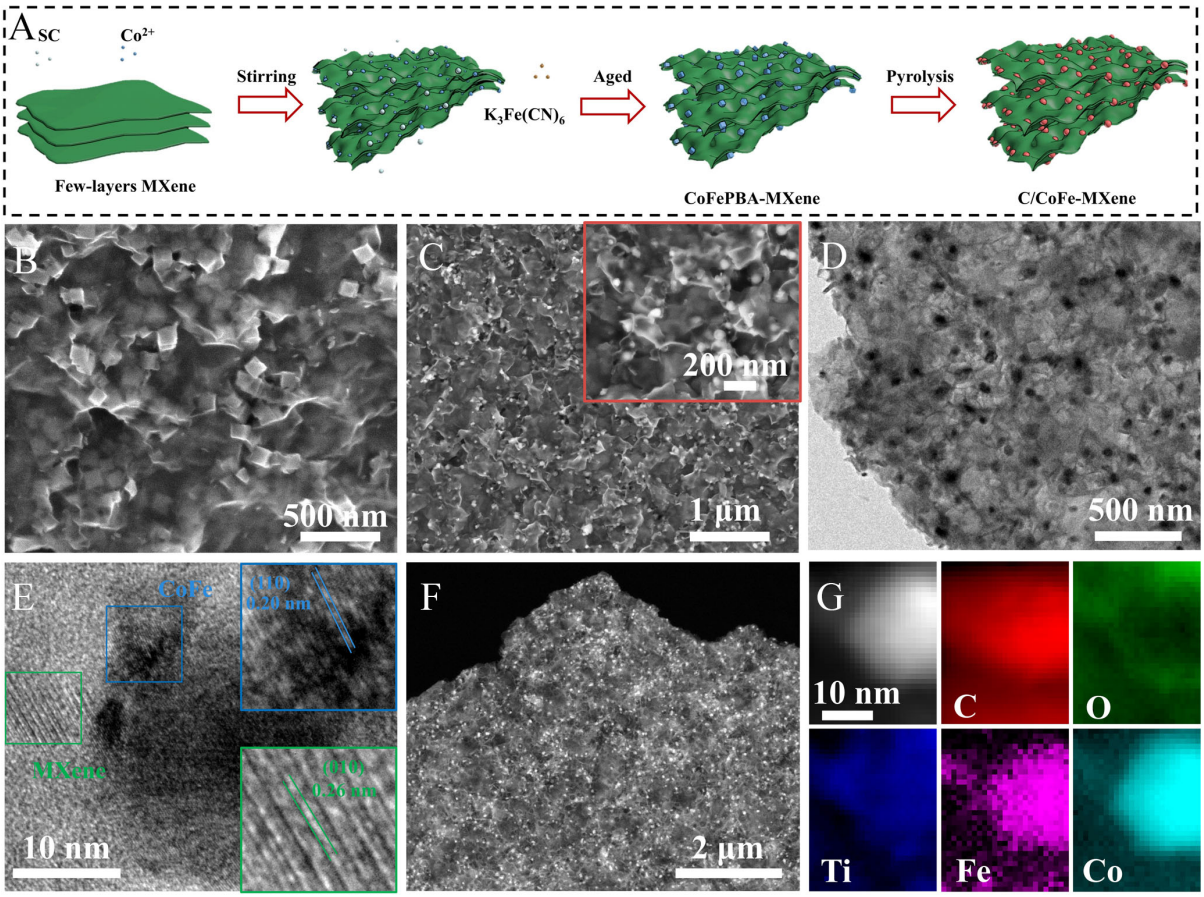

Figure 1. (A) Schematic illustration for the synthesis of C/CoFe-MXene. SEM images of (B) CoFePBA-MXene and (c) C/CoFe-MXene; Inset in (C) is the magnified image; (D) TEM image; (E) HRTEM image; (F) HAADF-STEM image and (G) corresponding EELS elemental mappings of C/CoFe-MXene. SEM: Scanning electron microscopy; TEM: transmission electron microscopy; HAADF-STEM: high-angle annular dark field scanning transmission electron microscopy; HRTEM: high resolution transmission electron microscopy; EELS: electron energy-loss spectroscopy.

resolution TEM images [Figure 1E] show that the C/CoFe alloy forms a distinct heterostructure with MXene. The lattice spacing of 0.20 nm and 0.26 nm are associated with the (110) plane of CoFe alloy and the (010) plane of MXene. A high-angle annual dark-field scanning transmission electron microscopy (HAADF-STEM) image [Figure 1F] further demonstrates that the C/CoFe alloy is uniformly distributed on the MXene substrate and the mapping results [Figure 1G, Supplementary Figures 3 and 4] further prove the uniform distribution of Fe and Co elements.

Phase changes of the samples and interlayer spacing of MXene were characterized by XRD analysis. No Ti_3AlC_2 peaks are observed in the XRD pattern of few-layer MXene [Supplementary Figure 5 and Figure 2A], implying the complete etching of the MAX phase. The diffraction peaks at 5.58° correspond to (002) plane of few-layer MXene and the diffraction peaks of CoFe-PBA indicate that the precursor CoFe-PBA was transformed into the C/CoFe alloy after calcination. As presented in Figure 2A, the diffraction peaks at 44.9° and 65.3° can be well assigned to the (110) and (200) planes of CoFe alloy (JCPDS No. 49 -1568). The other diffraction peaks in C/CoFe-MXene correspond to the MXene phase, where the diffraction peaks of 6.3° and 28.3° correspond to (002) and (008) planes, respectively, and the remaining peaks correspond to {010} and {016} plane families[23]. Among them, the (002) peak of the C/CoFe-MXene is shifted to the right compared to pristine MXene (5.6°), corresponding to the shrinkage of interlayer spacing

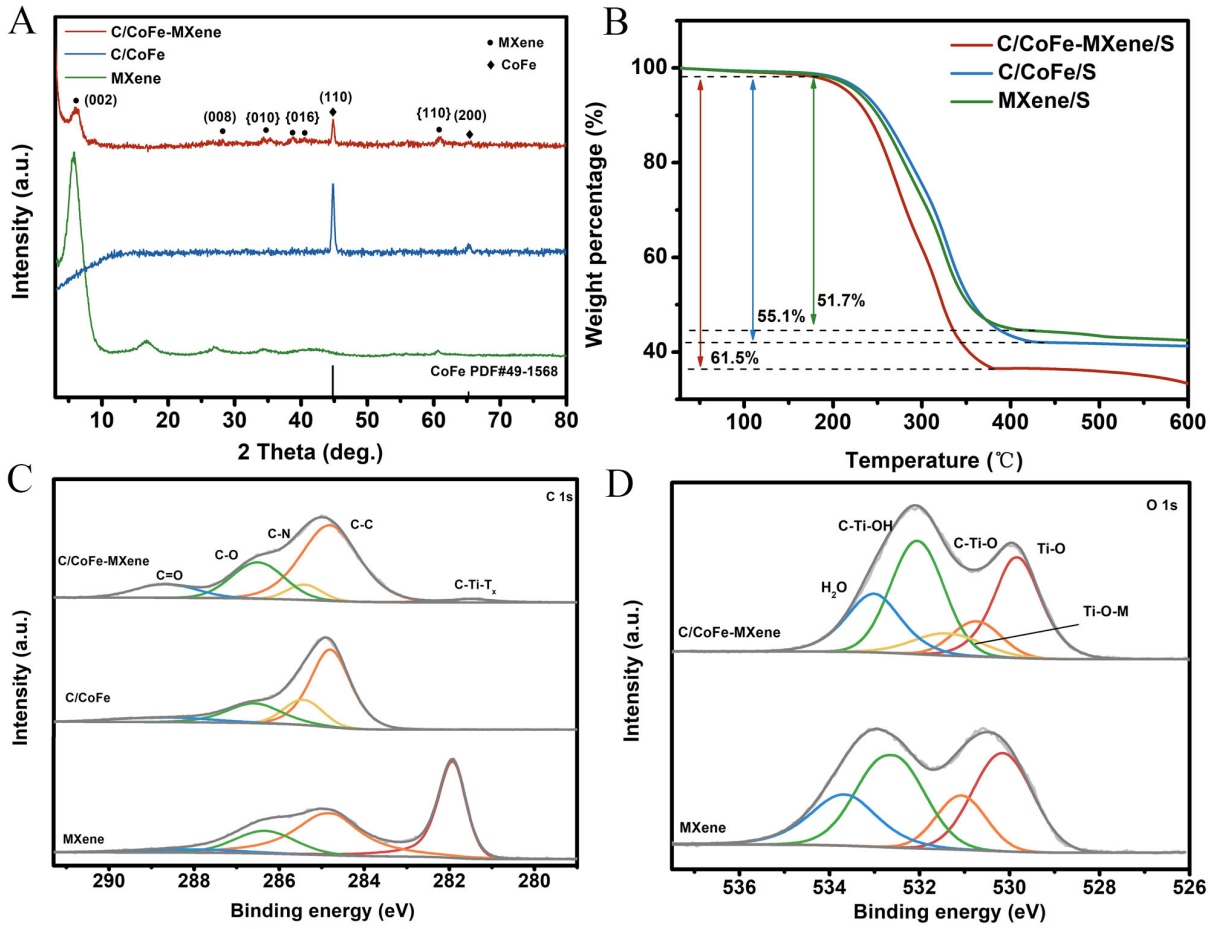

Figure 2. XRD patterns of (A) C/CoFe-MXene, C/CoFe and MXene; (B) TGA curves of C/CoFe-MXene/S, C/CoFe/S and MXene/S; High-resolution (C) C 1s and (D) O 1s XPS spectra. XRD: X-ray diffraction; TGA: thermogravimetric analysis; XPS: X-ray photoelectron spectroscopy.

of MXene, which is due to the loss of interstitial water molecules during calcination[24]. The appearance of the remaining peaks is due to the random orientations of MXene sheets during the self-assembly process, implying that the C/CoFe-MXene composite forms a good three-dimensional structure. As shown in Supplementary Figure 6, Raman spectra show that C/CoFe-MXene has the characteristic peaks of MXene and defective carbon of C/CoFe alloy, which further indicates that MXene and C/CoFe alloy are well combined. The N_2 adsorption-desorption analysis shows significant hysteresis characteristics of C/CoFe-MXene in Supplementary Figure 7A. According to the Brunauer-Emmett-Teller (BET) method, the specific surface area of C/CoFe-MXene is 125.8 $m^2 g^{-1}$, which is larger than that of MXene (23.9 $m^2 g^{-1}$) and C/CoFe (99.0 $m^2 g^{-1}$). In Supplementary Figure 7B, the specific pore volume of C/CoFe-MXene increased obviously, and the pore distribution indicated abundant macropores and mesopores in the C/CoFe-MXene matrix. Therefore, the *in-situ* assembly of C/CoFe alloy is beneficial to effectually inhibit the restacking and agglomeration of 2D MXene. This also allows C/CoFe-MXene to load with more sulfur, as confirmed in Figure 2B, where the C/CoFe-MXene with three-dimensional structure can load 61.5 wt% sulfur, higher than that of the other samples, further demonstrating the superiority of self-assembled three-dimensional structures.

XPS measurement was conducted to further characterize the chemical states and bonds of MXene, C/CoFe and C/CoFe-MXene. In Figure 2C, the C 1s XPS spectrum of C/CoFe-MXene shows some typical predominant peaks at 281.5 eV, 284.8 eV, 285.4 eV, 286.5 eV and 288.6 eV, which originate from C-Ti-T_x, C-C, C-N, C-O and C=O, respectively[25]. The O 1s XPS spectrum [Figure 2D] shows five predominant peaks at 529.8 eV, 530.7 eV, 531.4 eV, 532.1 eV and 533.0 eV, which correspond to Ti-O, C-Ti-O, Ti-O-M (M=Co, Fe), C-Ti-OH and H_2O, respectively[26]. Compared with pristine MXene, the emergence of Ti-O-M (M=Co, Fe) peak in C/CoFe-MXene means that the Co and Fe in the CoFe alloy are bonded to the oxygen terminals on the surface of the MXene to form a heterostructure[27,28]. To further verify the coupling effect between CoFe alloy and MXene, we performed high-resolution XPS tests [Supplementary Figure 8]. In the Co 2p XPS spectra of C/CoFe-MXene, the two peaks at 778.4 eV and 795.3 eV can be ascribed to zero-valence, originating from Co element in the CoFe alloy. The peaks at 782.7/798.1 eV and 780.9/796.5 eV are ascribed to the ionic states, demonstrating that metal ions are bonded with oxygen and nitrogen. The bonding of metal with oxygen can be interpreted as the combination of metal ions with oxygen terminals on the surface of MXene and oxygen absorbed on the surface of alloys. The residual nitrogen element after pyrolysis of CoFe-PBA will combine with the metal ion to form the metal nitrogen bond[29,30]. Similar to Co 2p, the Fe 2p XPS spectrum displays Fe^0 (707.7/721.0 eV), Fe^{2+} (710.4/723.8 eV), Fe^{3+} (713.4/726.5 eV) and two satellite peaks (717.9/731.3 eV)[31]. Notably, compared with the C/CoFe, the main peaks of C/CoFe-MXene shift towards higher binding energies, suggesting the strong coupling effect between C/CoFe alloy and MXene[32], which can account for the electron transfer between Co, Fe and Ti[33,34]. Besides, the Ti 2p XPS spectrum exhibits feature spectra of MXene referring to C-Ti-T_x (455.2/461.2 eV), Ti^{2+} (456.2/462.0 eV), Ti^{3+} (457.5/463.0 eV), Ti-O (459.3/464.8 eV) bonds and C-Ti-F_x (460.0/465.7 eV) bonds[35]. By comparing with Ti 2p of MXene [Supplementary Figure 8C], the intensity of Ti-O from C/CoFe-MXene is increased, because functional groups such as hydroxyl groups (-OH) will be converted into oxygen functional groups after calcination[36], which is also conducive to the bonding of metal ions from C/CoFe alloy to form a stable heterostructure.

The adsorption effect of C/CoFe-MXene toward NaPSs can also be evaluated by NaPS adsorption experiment and related UV-vis absorption spectra. As shown in Figure 3A, the color of NaPS solution adsorbed by C/CoFe-MXene became transparent, while brown color was retained in the other two samples, which demonstrates the strongest NaPS adsorption capability of C/CoFe-MXene. The result of the UV-vis spectrum also shows that the peak intensity of NaPSs is lower than that of other two samples and the blank, double confirming the best NaPS adsorption capability in C/CoFe-MXene. The high-resolution XPS spectrum is applied to reveal the interaction of C/CoFe-MXene with the polysulfide. As shown in Figure 3B and C, and Supplementary Figure 9, after adsorption of Na_2S_6, the Co^{2+}/Co^{3+} and Fe^{2+}/Fe^{3+} peaks shift slightly to lower binding energies, which means that the Na_2S_6 species transfer electrons to Co and Fe atoms. This can also be considered to the formation of Co-S/Fe-S bonds due to the Lewis acid-based role[37]. In Ti 2p XPS spectrum of C/CoFe-MXene [Supplementary Figure 10], the increased intensity of the Ti^{2+} and Ti^{3+} may be related to the strong interaction of Ti atoms with polysulfides[38]. Furthermore, in the S 2p XPS spectrum [Figure 3D], the terminal sulfur (S_T^{-1}) and bridging sulfur (S_B^0) atoms were located at 161.9/163.1 eV and 164.0/164.9 eV, respectively. The polythionate (168.9 eV) and thiosulfate (167.7 eV) peaks were located at higher binding energy, which are formed when the Na_2S_6 comes into contact with samples. Obviously, the intensity of these two peaks in C/CoFe-MXene is higher than that of other samples, which means more thiosulfate and polythionate were produced[39]. Overall, the C/CoFe-MXene exhibits the strongest interaction ability with polysulfides after adsorption. Furthermore, to verify the electrocatalytic activity for NaPSs on the surface of MXene, C/CoFe and C/CoFe-MXene, symmetrical cells with different electrodes were assembled by using Na_2S_6-containing electrolytes at the scanning rates from 1.0 mV s^{-1} to 10 mV s^{-1} [Supplementary Figure 11]. The CV curve of the C/CoFe-MXene exhibits higher current response than that of the MXene and C/CoFe [Figure 3E], demonstrating that the C/CoFe-MXene with better

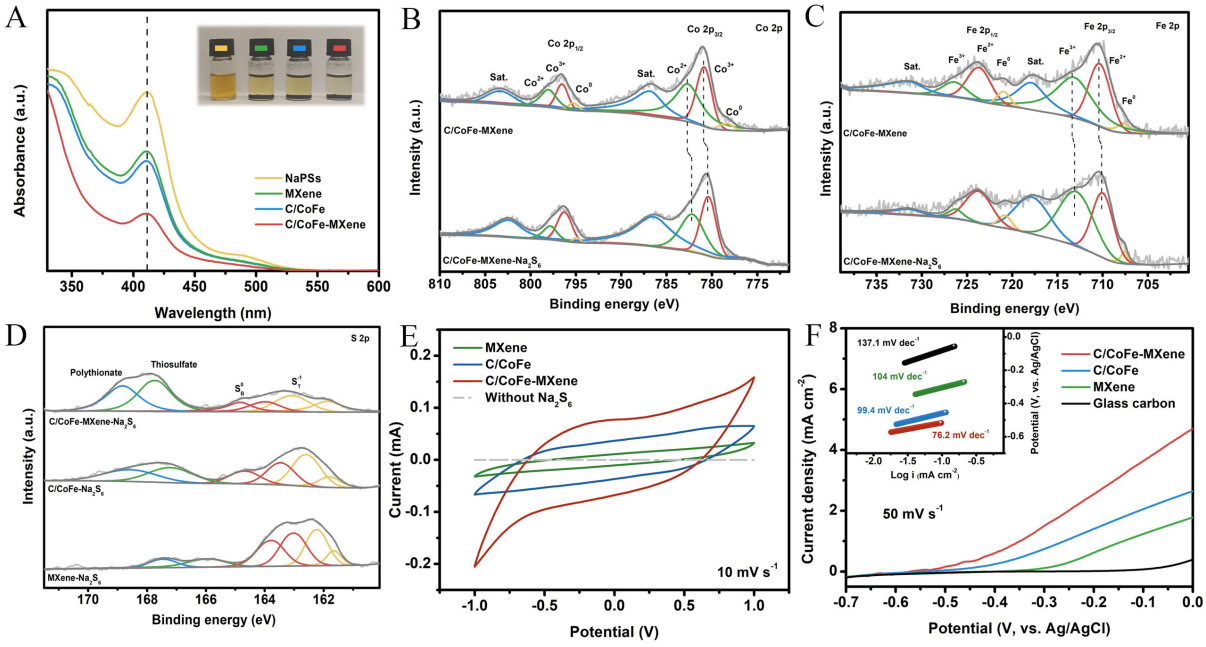

Figure 3. (A) UV-vis spectra after adsorption between NaPSs with different samples and digital photos (inset); High-resolution (B) Co 2p; (C) Fe 2p XPS spectra of C/CoFe-MXene before and after adsorption; High-resolution (D) S 2p XPS spectra of C/CoFe-MXene, C/CoFe and MXene after adsorption; (E) CV curves of symmetric batteries with different samples at 10 mV s^{-1}; (F) LSV curves of Na_2S oxidation and corresponding Tafel plots (inset). UV-vis: Ultraviolet-visible; XPS: X-ray photoelectron spectroscopy; CV: cyclic voltammetry; LSV: linear sweep voltammetry; NaPSs: sodium polysulfides.

electrocatalytic activity can accelerate conversion of polysulfides[40]. LSV tests were performed to study the oxidation kinetics of Na_2S on different samples. As shown in Figure 3F, a C/CoFe-MXene electrode delivers the lowest potential and highest current response, indicating that C/CoFe-MXene has better catalytic activity and can promote the conversion of polysulfides with the lowest activation energy. By fitting the Tafel curves, the C/CoFe-MXene delivers the smallest Tafel slope of 76.2 mV dec^{-1} by comparing with glass carbon (137.1 mV dec^{-1}), MXene (104 mV dec^{-1}) and C/CoFe (99.4 mV dec^{-1}), revealing the fastest sulfur conversion kinetics in C/CoFe-MXene electrode[41].

CV measurements were employed to examine the electrochemical behaviors of the cell with C/CoFe-MXene and other cathodes. Figure 4A exhibits the CV tests for the initial five cycles at 0.1 mV s^{-1}. For the CV curve at the first cycle, a cathodic peak at 2.1 V was observed and is attributed to the conversion of S_8 to Na_2S_x ($4 \le x \le 8$). The cathodic peak at 0.75 V is mainly attributed to the conversion of Na_2S_x ($4 \le x \le 8$) to Na_2S_x ($x \le 2$). In addition, the formation of surface solid electrolyte interphase (SEI) film and related side reactions are also involved at this stage[42]. In the subsequent cycles, two cathodic peaks at about 1.5 V and 1.0 V and an anodic peak around 2.0 V have emerged, which are interpreted as the conversion of long-chain NaPSs to Na_2S_4 and eventually into Na_2S and the reversible oxidation of short-chain NaPSs to long-chain NaPSs during charge procession, respectively[43]. The first five CV curves of the other two samples are compared in Supplementary Figure 12. In Figure 4B and C and Supplementary Figure 13, the C/CoFe-MXene cathode under 2.0 mg cm^{-2} sulfur loading achieves excellent rate performance with specific capacities of 1,496 mAh g^{-1}, 798 mAh g^{-1}, 576 mAh g^{-1}, 463 mAh g^{-1}, 379 mAh g^{-1}, 320 mAh g^{-1} and 270 mAh g^{-1} at 0.2 C, 0.5 C, 1.0 C, 2.0 C, 3.0 C, 4.0 C, and 5.0 C, respectively. Clearly, the C/CoFe-MXene cathode exhibits higher capacities at high current densities than other samples. In Figure 4D, the long-term cycle stability of the cells with different cathodes was evaluated at 1 C. Specifically, the C/CoFe-MXene cathode delivered an initial specific capacity of 572 mAh g^{-1} and retained a reversible capacity of

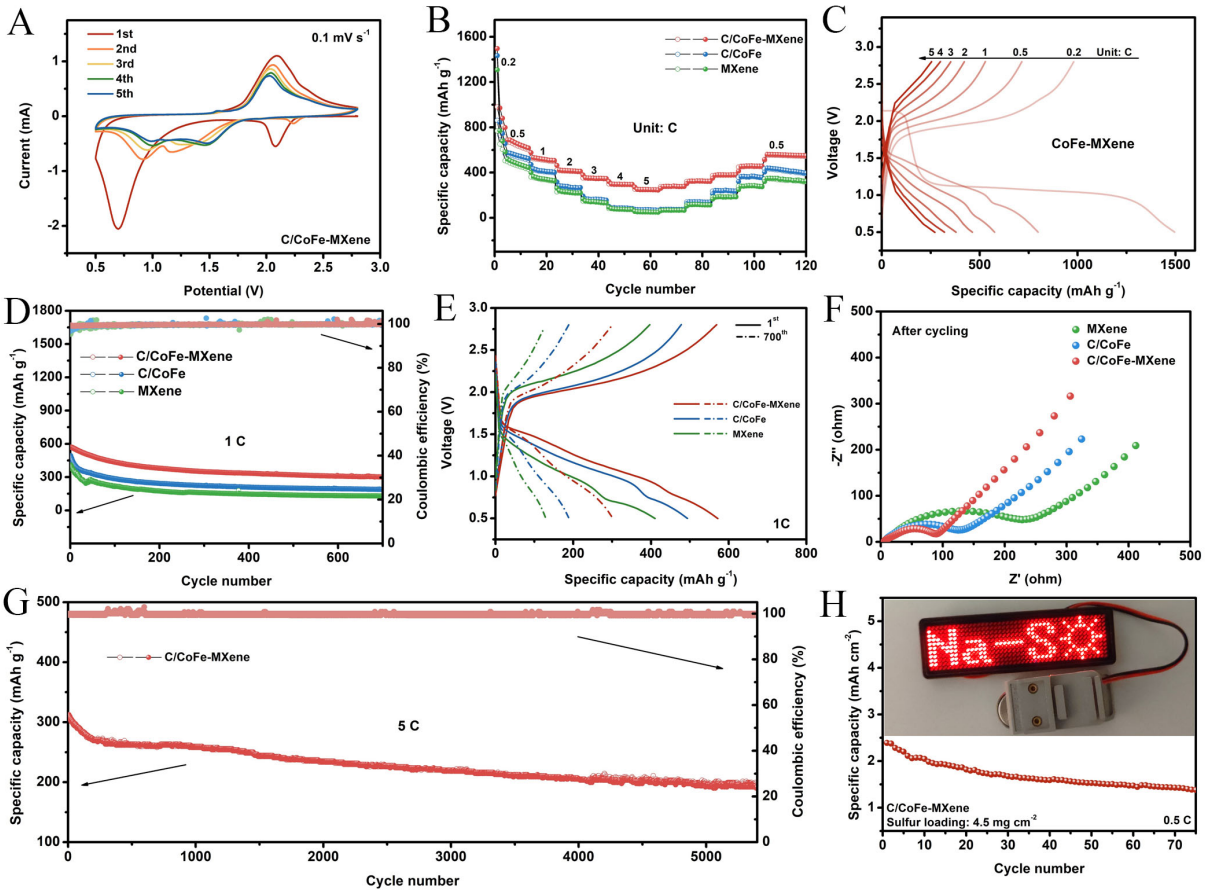

Figure 4. (A) The first five CV curves of the cell with C/CoFe-MXene electrode; (B) Rate capability of different electrodes and (C) galvanostatic charge/discharge profiles of the cell with C/CoFe-MXene electrode at different rates; (D) Cycling performance of the cell with different electrodes under 1 C; (E) Galvanostatic charge/discharge profiles of the cell at the 1st and the 700th cycle under 1 C; (F) Nyquist plots after cycling at 1 C; (G) Ultralong-term cycling performance of C/CoFe-MXene electrode at 5 C; (H) Cycling performance of C/CoFe-MXene/S with high sulfur loading at 0.5 C and inset digital photo of a light-emitting diode (LED) powered by the cell. CV: Cyclic voltammetry.

302 mAh g^{-1} after 700 cycles, which corresponds to a slow capacity decay rate of 0.0912% per cycle. In contrast, the initial specific capacity of C/CoFe and MXene cathodes is 494 mAh g^{-1} and 410 mAh g^{-1}, and cycled reversible capacity is 189 mAh g^{-1} and 130 mAh g^{-1}, which show capacity fading rate of 0.14% and 0.16% per cycle, respectively. Figure 4E presents the galvanostatic charge-discharge curves of the first cycle and the 700th cycle under 1.0 C. The C/CoFe-MXene cathode exhibits a smaller voltage gap than other cathodes, further demonstrating that C/CoFe-MXene possesses superior electrocatalytic activity toward the conversion of NaPSs. The EIS analysis of the batteries after 700 cycles [Figure 4F] reveals that C/CoFe-MXene unfolds the smallest charge transfer resistance (R_{ct}) of 83.4 Ω, compared with C/CoFe (118.6 Ω) and MXene (220.9 Ω), suggesting that the redox kinetics of NaPS conversions are significantly improved by the constructed heterostructure. Additionally, the electrochemical performance of batteries with different sulfur loadings under 1C was shown in Supplementary Figure 14. To further investigate the tolerance of the electrode under high current density, the cell with C/CoFe-MXene electrode was evaluated at 5 C [Figure 4G]. To be more specific, the C/CoFe-MXene cathode displayed a specific capacity of 310 mAh g^{-1} and retained reversible capacity of 192 mAh g^{-1} after 5,400 cycles with a slow capacity fading rate of 0.0089% per cycle. It exhibits excellent long-cycle stability compared to other current materials [Supplementary Table 1]. Figure 4H shows that the C/CoFe-MXene cathode still maintains good cycling stability when the

sulfur loading increased to 4.5 mg cm^{-2}, further revealing the advantages of the structured C/CoFe-MXene cathode. The advantages of the C/CoFe-MXene's excellent three-dimensional structure were further verified by the SEM and characterizations of the electrode after cycling [Supplementary Figure 15].

Na^+ diffusion rate plays a crucial role for the redox kinetics of NaPSs, which has been investigated by CV measurements and GITT of RT Na-S batteries using C/CoFe-MXene, C/CoFe and MXene electrodes. As shown in Figure 5A-C, the CV curves with different scan rates from 0.1 mV s^{-1} to 1.0 mV s^{-1} indicate that the C/CoFe-MXene electrode exhibits less potential polarization compared to other electrodes with the increased scan rates, suggesting superior redox reversibility of C/CoFe-MXene. The relationship between the peak current (i) and scan rate (v) and its equivalent form are given by:

$$i = av^b \tag{2}$$

$$\log(i) = b\log(v) + \log(a) \tag{3}$$

Where b is a constant. A b value of 0.5 suggests that the electrochemical process is limited by electrolyte ion diffusion, while b=1 represents a non-diffusion controlled capacitive process where surface capacitance is dominant in the charge storage mechanism[44]. According to the fitted plots in Figure 5A inset, the calculated b values are 0.764 and 0.623 for the cathodic peak/ anodic peak, confirming a hybrid surface-controlled and diffusion-controlled charge storage feature of C/CoFe-MXene electrode. On the other hand, GITT curves of C/CoFe-MXene, C/CoFe and MXene reveal superior performance of heterostructures constructed by CoFe alloy and MXene on the charge transfer properties during the sodiation and desodiation processes [Figure 5D]. The sodium-ion diffusion coefficient D_{Na+} (cm^2 s^{-1}) was determined through GITT results. The value of D_{Na+} was calculated using the Fick's second law:

$$D = \frac{4}{\pi\tau}\left(\frac{m_B V_M}{M_B S}\right)^2\left(\frac{\Delta E_s}{\Delta E_\tau}\right)^2 \left(\tau \ll \frac{L^2}{D}\right) \tag{4}$$

where M_B represents the molar mass of active material, S means the electrode area, V_M equals the molar volume of the active materials, m_B describes the mass of active material, and τ denotes the current time[45]. To be more specific, the C/CoFe-MXene has higher Na^+ diffusion coefficient than the C/CoFe and MXene during the whole voltage range [Figure 5E], suggesting the heterostructure of C/CoFe-MXene is more beneficial to Na^+ diffusion. This also shows that low resistance and fast reaction kinetics are maintained throughout the charge-discharge process, which is also demonstrated by the *in-situ* EIS [Figure 5F and Supplementary Figure 16]. Specifically, after discharge to 1.0 V at the first discharge stage, there is a slight increase in resistance because the dissolved polysulfide in the electrolyte increases the concentration of the electrolysis[46]. When further discharged to 0.5 V, the resistance increases further, because the polysulfide is converted into solid sodium sulfide and deposited on the cathode surface. That is why there are two semicircles in the middle and low frequency ranges and the internal resistance of the battery reaches the maximum in this state. During the charging process, the resistance decreases first and then increases as sodium sulfide converts to polysulfide and then to solid sulfur. Similarly, the change in resistance during the second cycle of discharge is almost the same as during the first cycle of discharge, which further proves the reversible redox reaction of RT Na-S batteries in this system[47]. Additionally, compared to other samples, C/CoFe-MXene always maintained the smallest internal resistance throughout the charge-discharge process, which also shows that the C/CoFe-MXene is conducive to the catalytic conversion of polysulfides and thus faster reaction kinetics.

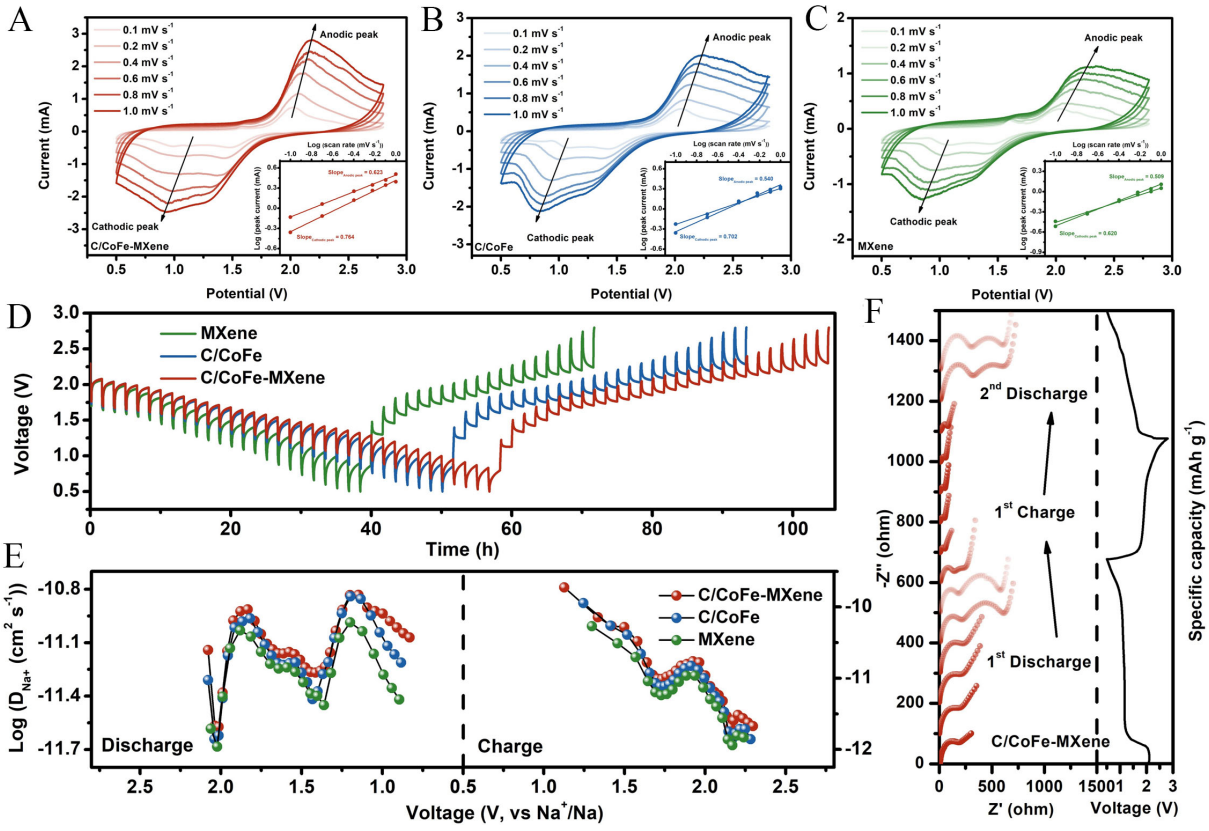

Figure 5. CV curves at different scan rates and corresponding linear fits of the peak current densities (inset) of the cell with (A) C/CoFe-MXene, (B) C/CoFe, and (C) MXene electrodes; (D) GITT profiles of RT Na-S batteries with different electrodes during discharge and charge processes and (E) corresponding Na^+ ion diffusion coefficients; (F) *In-situ* EIS plots of RT Na-S batteries with C/CoFe-MXene electrode at different states. CV: Cyclic voltammetry; GITT: galvanostatic intermittent titration technique; RT Na-S: room-temperature sodium-sulfur.

Density functional theory (DFT) calculations were carried out to elucidate the strong interaction between CoFe alloy and MXene, investigate the adsorption behavior of NaPSs on different substrates and reveal their electrocatalytic functionalities during sulfur conversion. Supplementary Figure 17 displayed the simulated clean surface of MXene, CoFe and CoFe-MXene. The reduced conversion process of NaPSs is divided into six steps[48,49], and their corresponding structures in the side view are shown in Figure 6A and Supplementary Figure 18. By comparing with the binding energy of NaPSs on different substrates [Figure 6B and Supplementary Table 2], the CoFe-MXene is found to possess superior anchoring ability for polysulfides. From the calculated differential charge density [Figure 6C], the electrons are transferred from CoFe alloy to MXene in heterointerface, suggesting a self-built internal electric field that could accelerate the electron/ion transport during the charge/discharge process[50,51]. These results are consistent with the analysis of the XPS. The density of states (DOS) of the CoFe-MXene, CoFe and MXene [Figure 6D] reveals that CoFe-MXene composite possesses increased DOS at Fermi level compared with CoFe and MXene, confirming its higher metallic conductivity. This also indicated the strong coupling effect between CoFe and MXene. The optimized adsorption configurations in the top view, showing the interactions between NaPS species and CoFe-MXene, CoFe, and MXene, are displayed in Figure 6E and Supplementary Figure 19. Furthermore, Gibbs free energies (ΔG) are estimated for the conversion of NaPS species on three substrates. As shown in Figure 6E, the transformation from S_8 to Na_2S_8 is spontaneous, while every conversion step from Na_2S_8 to Na_2S faces an energy uphill. In particular, the conversion from Na_2S_4 to Na_2S_2 exhibits an extraordinarily high-energy barrier, which can be regarded as the rate-limiting step during the discharge process[52]. The

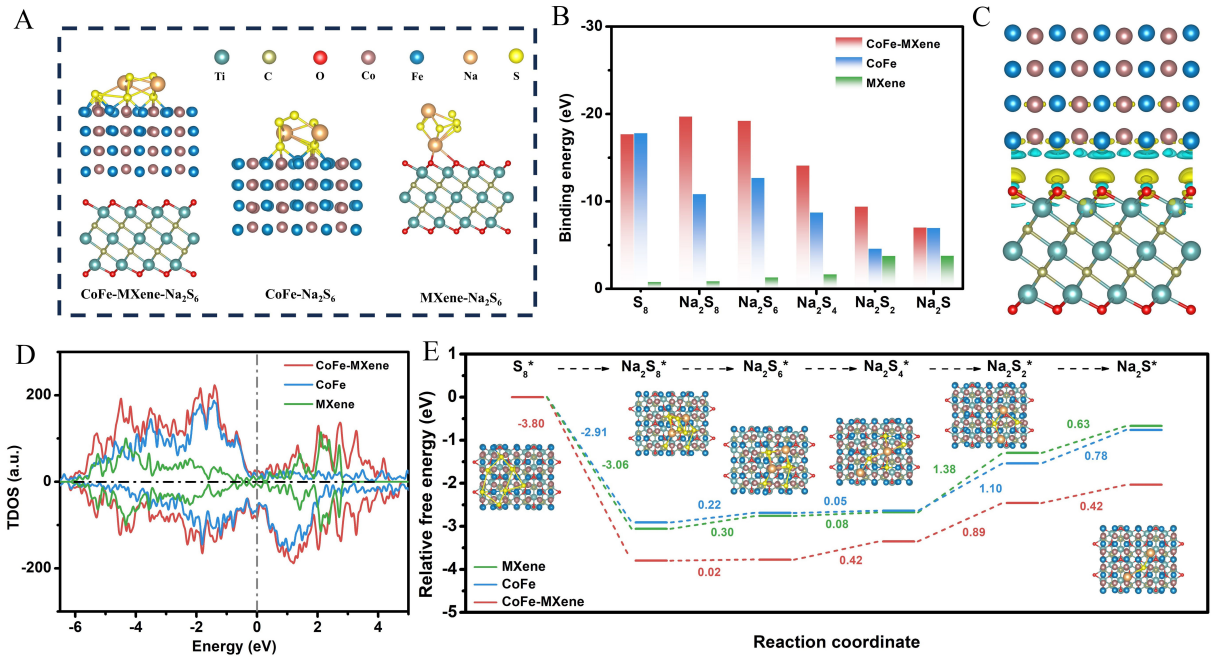

Figure 6. (A) Optimized adsorption conformations of Na_2S_6; (B) Binding energy of NaPSs species; (C) Differential charge density distribution at interface of CoFe-MXene, yellow and blue regions indicate electron accumulation and depletion, respectively. (D) Density of states; (E) Gibbs free energy profiles of NaPSs species on the CoFe-MXene, CoFe and MXene. NaPSs: Sodium polysulfides.

largest ΔG values for CoFe-MXene, CoFe and MXene surfaces are 0.89 eV, 1.10 eV and 1.38 eV, respectively. Obviously, the CoFe-MXene exhibits the lowest ΔG barrier, which proves that the reduction process of sulfur could be boosted on CoFe-MXene surface from the perspective of thermodynamics. These results demonstrate that heterostructure from the CoFe-MXene nanocomposite exerts a synergistic catalytic effect that promotes the whole conversion and shows better reaction kinetics.

CONCLUSIONS

In summary, C/CoFe alloys embedded on MXene substrate catalysts were designed via an *in situ* growth strategy as a sulfur host for RT Na-S batteries. Specifically, compared to the performance of C/CoFe and MXene, the C/CoFe-MXene delivered an impressive specific capacity and an ultralow capacity decay of 0.0089% per cycle at 5 C, demonstrating high tolerance at high current densities. Through comprehensive systemic characterizations on structural features, chemical interactions, and electrochemical behavior, the structure-property relationship in the dynamic electrode reaction process was revealed. Structurally, the introduction of C/CoFe alloys facilitates the assembly of three-dimensional structures with MXene, allowing MXene to expose more active surface-supported nanoalloys to form heterostructures. The C/CoFe alloy and MXene are connected by bonding, enhancing the stability of the catalyst under long-term cycles and high current density, preventing detachment and failure. Functionally, C/CoFe alloys act as potent catalysts for the adsorption and conversion of polysulfides. The heterogeneous interface between the C/CoFe alloy and MXene facilitates rapid ion transport, accelerates reaction kinetics, and improves rate performance. This work provides new insights into understanding the catalytic role of MXene-based supported nanoalloy catalysts during kinetic conversion.

DECLARATIONS

Authors' contributions

Methodology, characterization, data analysis, writing-original draft: Yu, X.
Characterization: Liang, K.; Liu, S.; Li, L.; Zhu, Y.
Writing-review and editing: Li, H.
Conceptualization, supervision, writing-review and editing, funding resources: Huang, H.
All authors have given approval to the final version of the manuscript.

Availability of data and materials

All data are available in the manuscript and the Supplementary Materials.

Financial support and sponsorship

This work was supported by the Science and Technology Program of Guangdong Province of China (2021B1515130010). Yu, X. thanks the financial support from the Research Institute for Smart Energy, the Hong Kong Polytechnic University.

Conflicts of interest

All authors declared that there are no conflicts of interest.

Ethical approval and consent to participate

Not applicable.

Consent for publication

Not applicable.

REFERENCES

1. Sun, Y.; Liu, N.; Cui, Y. Promises and challenges of nanomaterials for lithium-based rechargeable batteries. *Nat. Energy.* **2016**, *1*, 1671. DOI
2. Pan, H.; Hu, Y.; Chen, L. Room-temperature stationary sodium-ion batteries for large-scale electric energy storage. *Energy. Environ. Sci.* **2013**, *6*, 2338-60. DOI
3. Zhao, L.; Tao, Y.; Zhang, Y.; et al. A critical review on room-temperature sodium-sulfur batteries: from research advances to practical perspectives. *Adv. Mater.* **2024**, *36*, 2402337. DOI
4. Jin, F.; Wang, B.; Wang, J.; et al. Boosting electrochemical kinetics of S cathodes for room temperature Na/S batteries. *Matter* **2021**, *4*, 1768-800. DOI
5. Zhang, S.; Yao, Y.; Yu, Y. Frontiers for room-temperature sodium-sulfur batteries. *ACS. Energy. Lett.* **2021**, *6*, 529-36. DOI
6. Kumar Saroja AP, Xu Y. Carbon materials for Na-S and K-S batteries. *Matter* **2022**, *5*, 808-36. DOI
7. Yang, J.; Han, H.; Repich, H.; et al. Recent progress on the design of hollow carbon spheres to host sulfur in room-temperature sodium-sulfur batteries. *New. Carbon. Mater.* **2020**, *35*, 630-45. DOI
8. Yang, X.; Luo, J.; Sun, X. Towards high-performance solid-state Li-S batteries: from fundamental understanding to engineering design. *Chem. Soc. Rev.* **2020**, *49*, 2140-95. DOI PubMed
9. Xiao, Y.; Zheng, Y.; Yao, G.; et al. Defect engineering of a TiO_2 anatase/rutile homojunction accelerating sulfur redox kinetics for high-performance Na-S batteries. *Dalton. Trans.* **2024**, *53*, 8168-76. DOI
10. Ye, X.; Ruan, J.; Pang, Y.; et al. Enabling a stable room-temperature sodium-sulfur battery cathode by building heterostructures in multichannel carbon fibers. *ACS. Nano.* **2021**, *15*, 5639-48. DOI
11. Asif, M.; Ali, Z.; Qiu, H.; Rashad, M.; Hou, Y. Confined polysulfide shuttle by nickel disulfide nanoparticles encapsulated in graphene nanoshells synthesized by cooking oil. *ACS. Appl. Energy. Mater.* **2020**, *3*, 3541-52. DOI
12. Sadaqat, A.; Ali, G.; ul, H. M.; Liaqat, A.; Khalid, S.; Farooq, K. M. Binary Co_3S_4/SnS chalcogenide composites anchored on graphene oxide and carbon nanotubes as anodes for Na-ion batteries. *Appl. Surf. Sci.* **2024**, *665*, 160323. DOI
13. Guo, Q.; Ma, Y.; Chen, T.; et al. Cobalt sulfide quantum dot embedded N/S-doped carbon nanosheets with superior reversibility and rate capability for sodium-ion batteries. *ACS. Nano.* **2017**, *11*, 12658-67. DOI

14. Wang, L.; Wang, H.; Zhang, S.; et al. Manipulating the electronic structure of nickel via alloying with iron: toward high-kinetics sulfur cathode for Na-S batteries. *ACS. Nano.* **2021**, *15*, 15218-28. DOI
15. Dai, X.; Wang, Z.; Wang, X.; et al. MXene-based sodium-sulfur batteries: synthesis, applications and perspectives. *Rare. Met.* **2025**, *44*, 1522-55. DOI
16. Huo, X.; Liu, Y.; Li, R.; Li, J. Two-dimensional $Ti_3C_2T_x$@S as cathode for room temperature sodium-sulfur batteries. *Ionics* **2019**, *25*, 5373-82. DOI
17. Reddy, B.; Cho, G.; Reddy, N.; et al. Layered-like structure of TiO_2-Ti_3C_2 Mxene as an efficient sulfur host for room-temperature sodium-sulfur batteries. *J. Alloys. Compd.* **2021**, *883*, 160910. DOI
18. Zhang, Y.; Ma, C.; He, W.; et al. MXene and MXene-based materials for lithium-sulfur batteries. *Prog. Nat. Sci. Mater. Int.* **2021**, *31*, 501-13. DOI
19. Zhang, S.; Zhong, N.; Zhou, X.; et al. Comprehensive design of the high-sulfur-loading Li-S battery based on MXene nanosheets. *Nano-Micro. Lett.* **2020**, *12*, 112. DOI
20. Zhao, W.; Lei, Y.; Zhu, Y.; et al. Hierarchically structured $T_{i3}C_2T$ MXene paper for Li-S batteries with high volumetric capacity. *Nano. Energy.* **2021**, *86*, 106120. DOI
21. Li, H.; Zhou, H.; Zhuang, L.; Liu, T.; Han, W.; Huang, H. Enhanced ion diffusion in flexible Ti_3C_2TX MXene film for high-performance supercapacitors. *Adv. Energy. Sustain. Res.* **2022**, *3*, 2100216. DOI
22. Yu, X.; Yang, Y.; Si, L.; Cai, J.; Lu, X.; Sun, Z. $V_4C_3T_X$ MXene: first-principles computational and separator modification study on immobilization and catalytic conversion of polysulfide in Li-S batteries. *J. Colloid. Interface. Sci.* **2022**, *627*, 992-1002. DOI
23. Ghidiu, M.; Barsoum, M. W. The {110} reflection in X-ray diffraction of MX ene films: misinterpretation and measurement via non-standard orientation. *J. Am. Ceram. Soc.* **2017**, *100*, 5395-9. DOI
24. Liu, W.; Zheng, Y.; Zhang, Z.; et al. Ultrahigh gravimetric and volumetric capacitance in $Ti_3C_2T_x$ MXene negative electrode enabled by surface modification and in-situ intercalation. *J. Power. Sources.* **2022**, *521*, 230965. DOI
25. Feng, J.; Liu, W.; Shi, C.; et al. Enabling fast diffusion/conversion kinetics by thiourea-induced wrinkled N, S co-doped functional MXene for lithium-sulfur battery. *Energy. Storage. Mater.* **2024**, *67*, 103328. DOI
26. Wang, Z.; Jiang, H.; Wei, C.; et al. Ultrasmall CoFe bimetallic alloy anchored on fluoride-free MXene by one-pot etching strategy for the barrier-adsorption-catalyst functions of polysulfides in lithium-sulfur batteries. *Adv. Funct. Mater.* **2024**, *34*, 2315178. DOI
27. Hui, X.; Zhao, R.; Zhang, P.; Li, C.; Wang, C.; Yin, L. Low-temperature reduction strategy synthesized Si/Ti_3C_2 MXene composite anodes for high-performance Li-ion batteries. *Adv. Energy. Mater.* **2019**, *9*, 1901065. DOI
28. Huang, P.; Zhang, S.; Ying, H.; et al. Fabrication of Fe nanocomplex pillared few-layered $Ti_3C_2T_x$ MXene with enhanced rate performance for lithium-ion batteries. *Nano. Res.* **2021**, *14*, 1218-27. DOI
29. Mou, J.; Li, Y.; Liu, T.; et al. Metal-organic frameworks-derived nitrogen-doped porous carbon nanocubes with embedded Co nanoparticles as efficient sulfur immobilizers for room temperature sodium-sulfur batteries. *Small. Methods.* **2021**, *5*, 2100455. DOI
30. Qi, W.; Wu, W.; Cao, B.; Zhang, Y.; Wu, Y. Fabrication of CoFe/N-doped mesoporous carbon hybrids from Prussian blue analogous as high performance cathodes for lithium-sulfur batteries. *Int. J. Hydrogen. Energy.* **2019**, *44*, 20257-66. DOI
31. Wang, Y.; Zhu, L.; Wang, J.; Zhang, Z.; Yu, J.; Yang, Z. Enhanced chemisorption and catalytic conversion of polysulfides via CoFe@NC nanocubes modified separator for superior Li-S batteries. *Chem. Eng. J.* **2022**, *433*, 133792. DOI
32. Lu, C.; Li, A.; Zhai, T.; et al. Interface design based on Ti_3C_2 MXene atomic layers of advanced battery-type material for supercapacitors. *Energy. Storage. Mater.* **2020**, *26*, 472-82. DOI
33. Zhang, G.; Yang, H.; Zhou, H.; et al. MXene-mediated interfacial growth of 2D-2D heterostructured nanomaterials as cathodes for zn-based aqueous batteries. *Angew. Chem. Int. Ed.* **2024**, *63*, e202401903. DOI
34. Yu, M.; Zhou, S.; Wang, Z.; Zhao, J.; Qiu, J. Boosting electrocatalytic oxygen evolution by synergistically coupling layered double hydroxide with MXene. *Nano. Energy.* **2018**, *44*, 181-90. DOI
35. Li, H.; Fan, K.; Xiong, P.; et al. Selective grafting of phosphorus onto Ti_3C_2Tx MXene enables a two-proton process and enhanced charge storage. *J. Mater. Chem. A.* **2024**, *12*, 3449-59. DOI
36. He, Y.; Zhao, Y.; Zhang, Y.; et al. Building flexibly porous conductive skeleton inlaid with surface oxygen-dominated MXene as an amphiphilic nanoreactor for stable Li-S pouch batteries. *Energy. Storage. Mater.* **2022**, *47*, 434-44. DOI
37. Zhang, G.; Chen, X.; Yu, X.; et al. Crystalline-amorphous heterostructure on the phosphatized P-CoS_2/CNT for augmenting the catalytic conversion kinetics of Li-S batteries. *Chem. Eng. J.* **2024**, *488*, 150696. DOI
38. Yao, Y.; Wang, S.; Jia, X.; et al. Freestanding sandwich-like hierarchically TiS_2-TiO_2/Mxene bi-functional interlayer for stable Li-S batteries. *Carbon* **2022**, *188*, 533-42. DOI
39. Park, S. J.; Choi, Y. J.; Kim, H.; et al. Stable immobilization of lithium polysulfides using three-dimensional ordered mesoporous Mn_2O_3 as the host material in lithium-sulfur batteries. *Carbon. Energy.* **2024**, *6*, e487. DOI
40. Ou, L.; Mou, J.; Peng, J.; Zhang, Y.; Chen, Y.; Huang, J. Heterostructured Co/CeO_2-decorating N-doped porous carbon nanocubes as efficient sulfur hosts with enhanced rate capability and cycling durability toward room-temperature Na-S batteries. *ACS. Appl. Mater. Interfaces.* **2024**, *16*, 3302-10. DOI
41. Mou, J.; Li, Y.; Ou, L.; Huang, J. A highly-efficient electrocatalyst for room temperature sodium-sulfur batteries: assembled nitrogen-doped hollow porous carbon spheres decorated with ultrafine α-MoC_{1-x} nanoparticles. *Energy. Storage. Mater.* **2022**, *52*, 111-9. DOI
42. Liu, H.; Lai, W. H.; Yang, Q.; et al. Understanding Sulfur redox mechanisms in different electrolytes for room-temperature Na-S batteries. *Nano-Micro. Lett.* **2021**, *13*, 121. DOI

43. Tang, K.; Peng, X.; Zhang, Z.; et al. A highly dispersed cobalt electrocatalyst with electron-deficient centers induced by boron toward enhanced adsorption and electrocatalysis for room-temperature sodium-sulfur batteries. *Small* **2024**, *20*, e2311151. DOI
44. Zhou, X.; Yu, Z.; Yao, Y.; et al. A high-efficiency Mo_2C electrocatalyst promoting the polysulfide redox kinetics for Na-S batteries. *Adv. Mater.* **2022**, *34*, 2200479. DOI
45. Jiang, Y.; Yu, Z.; Zhou, X.; et al. Single-atom vanadium catalyst boosting reaction kinetics of polysulfides in Na-S batteries. *Adv. Mater.* **2023**, *35*, 2208873. DOI
46. Zhao, Z.; Yi, Z.; Li, H.; et al. Synergetic effect of spatially separated dual co-catalyst for accelerating multiple conversion reaction in advanced lithium sulfur batteries. *Nano. Energy.* **2021**, *81*, 105621. DOI
47. Wang, Y.; Wang, Y.; Xu, C.; et al. Phosphor-doped carbon network electrocatalyst enables accelerated redox kinetics of polysulfides for sodium-sulfur batteries. *ACS. Nano.* **2024**, *18*, 3839-49. DOI
48. Jayan, R.; Islam, M. M. Mechanistic insights into interactions of polysulfides at VS_2 interfaces in Na-S batteries: a DFT study. *ACS. Appl. Mater. Interfaces.* **2021**, *13*, 35848-55. DOI PubMed
49. Fang, D.; Ghosh, T.; Huang, S.; et al. Core-shell tandem catalysis coupled with interface engineering for high-performance room-temperature Na-S batteries. *Small* **2023**, *19*, 2302461. DOI
50. Yu, X.; Wang, N.; Sun, Z.; Shao, L.; Shi, X.; Cai, J. Separator modified by a caterpillar-like composite with interconnected N-doped carbon nanotubes decorated Co-MnO heterointerface enabling robust polysulfide adsorption and catalytic conversion for Li-S batteries. *Electrochim. Acta.* **2023**, *457*, 142497. DOI
51. Li, T.; Liang, L.; Chen, Z.; Zhu, J.; Shen, P. Hollow Ti_3C_2T MXene@$CoSe_2$/N-doped carbon heterostructured composites for multiphase electrocatalysis process in lithium-sulfur batteries. *Chem. Eng. J.* **2023**, *474*, 145970. DOI
52. Gao, W.; Song, B.; Zhang, Q.; He, J.; Wu, Y. 3D flower-like nanospheres constructed by transition metal telluride nanosheets as sulfur immobilizers for high-performance room-temperature Na-S batteries. *Small* **2024**, *20*, 2310225. DOI